


Research Article

Evaluating Pore Structure of Shale Reservoirs through Pore Space Multifractal Characterization

Quanqi Dai ^{1,2}, Yingfu He,^{1,2} Da Zheng,³ Yangwen Zhu,^{1,2} Rui Wang,^{1,2} Hongmin Yu,^{1,2} Yinbang Zhou,^{1,2} Guiwen Wang,⁴ Yafeng Li,⁵ and Hao Wu⁶

¹State Key Laboratory of Shale Oil and Gas Enrichment Mechanisms and Effective Development, Beijing, China

²Petroleum Exploration and Production Research Institute, SINOPEC, Beijing, China

³Research Institute of Petroleum Exploration & Development, PetroChina, Beijing, China

⁴College of Geosciences, China University of Petroleum-Beijing, Beijing, China

⁵Research Institute of Exploration and Exploitation, PetroChina Qinghai Oilfield Company, Dunhuang, China

⁶School of Earth Sciences, Lanzhou University, Lanzhou, China

Correspondence should be addressed to Quanqi Dai; daiqq0614@outlook.com

Received 14 September 2022; Revised 29 November 2022; Accepted 18 March 2023; Published 25 April 2023

Academic Editor: Wenming Ji

Copyright © 2023 Quanqi Dai et al. This is an open access article distributed under the Creative Commons Attribution License, which permits unrestricted use, distribution, and reproduction in any medium, provided the original work is properly cited.

Characteristics of pore structure are crucial to oil exploration and development in shale reservoirs, but practical evaluation of shale pore structure remains a longstanding challenge. In this study, based on nuclear magnetic resonance transverse relaxation time (T_2) spectra under water-saturated and irreducible conditions, total pore space and moveable fluid space were skillfully determined. Meanwhile, multifractal spectra were used to characterize T_2 distributions of total pore space and movable fluid space. The results show characteristic parameters of high probability measure areas of multifractal spectra (multifractal parameters) have strong negative correlations with T_2 geometric mean value, and average radii of pore and throat increase with a decrease in the multifractal parameters, indicating the shale reservoirs with low values of the multifractal parameters may have good pore structure. Moreover, clay mineral content has strong positive effects on the multifractal parameters. In contrast, (quartz+feldspar) mineral content negatively influences on the multifractal parameters. Finally, new accurate models for permeability estimation in core scale and well-logging scale of shales are both proposed based on the multifractal parameters, which are also applicable for the other reservoirs. Overall, this study is important and timely for evaluating pore structure and predicting permeability in shale reservoirs.

1. Introduction

The increasing global demand for energy resources guides the importance of the exploration and development of unconventional oil reservoirs [1–4]. Pore structure plays an essential role in the fluid occurrence and flow properties and is one of the main features for evaluating of shale reservoirs [5–9]. Compared with other oil reservoirs such as sandstone and carbonate reservoirs, the pore structure of shale reservoirs is more challenging to evaluate [6–11]. This is because the shale reservoirs are always characterized by various mineral compositions, resulting in complex pore throat connectivity and extreme heterogeneity of pore size

distributions [8, 10–13]. Thus, effectively evaluating the pore structure of shale reservoirs is necessary and meaningful.

Currently, many experimental methods can test the pore structure of rocks. Scanning electron microscopy (SEM) can visually represent the shapes of pores and throats [14–16]. The high-pressure mercury injection (HPMI) method can effectively characterize the distribution of connected pore sizes in the rocks [7, 17]. Relaxation time (T_2) spectra obtained from nuclear magnetic resonance (NMR) experiment can quantitatively characterize the pore size distributions without damaging rocks, and which is combined with a core centrifugation experiment, the distribution of pore spaces occupied by the movable fluid in the rock can be effectively characterized

[6, 18–20]. Nano and microcomputed tomography (CT) can also accurately characterize the three-dimensional distributions of pores and throats without damaging the rock [21–23]. However, for the shales with strong heterogeneous porous systems, it is difficult to directly use the characteristics of pore sizes and pore distributions obtained from the above experiments to evaluate their pore structure quantitatively.

The multifractal theory analyzes the fractal sets based on the fluctuations of local probability measure, which can reveal both global properties and detailed local information on pore size distribution [20, 21, 24]. In the energy industry, multifractal dimensions have been a powerful tool for evaluating the pore structure of rocks by characterizing the heterogeneity of pore size distributions. Due to the NMR experiment which can obtain the pore size distributions of rocks conveniently and accurately, many scholars have used NMR T_2 spectra to calculate the multifractal dimensions. Li et al. [25] revealed that the porosity of tectonically deformed coals strongly correlates with the multifractal dimensions based on the NMR experiment. Liu and Ostadhassan [26] used the multifractal characteristic of NMR T_2 spectra to evaluate the pore structure of tight sandstones. Zheng et al. [24] provided a novel method to evaluate the pore structure of coals by using multifractal dimensions to calculate the T_2 cutoff. However, there are few studies on the multifractal characterization of pore structure for the shales. Furthermore, these multifractal analysis methods based on the NMR experiment are limited to the core scale and are hard to be used in the well logging for the continuous longitudinal estimation of reservoir permeability.

For the shale reservoirs, the irregular distribution of pore size directly leads to the complex pore structure characteristics [27–29], so it is important to use the multifractal theory to evaluate the heterogeneity of pore size distribution and explain the physical meanings corresponding to the multifractal parameters of the shales. In addition, according to the fluid flow behavior in pores, the total pore space of shales can be divided into two parts: movable fluid space and irreducible fluid space [7, 30, 31]. Previous studies have generally conducted multifractal analysis on the pore size distribution of the total pore space obtained by the NMR T_2 spectra under water-saturated conditions [23–25]. It has been shown that there is a strong correlation between the characteristics of movable fluid space and the pore throat connectivity of rocks [6, 7, 31]. Unfortunately, few reports relate to the multifractal analysis of the movable fluid space of shales. Thus, it is necessary to analyze the relationships between the pore structure parameters and the multifractal parameters of the movable fluid space for the shales.

In this study, the main purpose is to investigate the pore structure characterization of the shale reservoirs based on the multifractal analysis of the NMR T_2 spectra. This represents a critical contribution to the oil exploration and development of shale reservoirs and will have practical applications within unconventional reservoirs worldwide. The study content is to (1) use the NMR T_2 distributions under water-saturated and irreducible conditions to determine the moveable fluid space of the shales; (2) understand the relationships between the multifractal parameters and

the pore structure parameters of the shales; (3) investigate the effects of the shale compositions on the multifractal parameters; and (4) propose a multifractal model for the permeability estimation of the shale reservoirs in well-logging scale.

2. Experimental and Multifractal Methods

2.1. Samples. In this study, core samples are collected from the upper part of Lower Ganchaigou Formation (E_3^2) shale reservoirs, which are located at the Yingxi area of the Yingxiongling tectonic belt in the Qaidam Basin, northwest China [26]. During the E_3^2 shale deposition, the water body was saline, and the lake plane frequently changed, resulting in typical shales with complex mineral compositions [32]. Moreover, there is strong heterogeneity in the E_3^2 shale reservoirs, which have low porosity and permeability [23, 33, 34]. A total of fifteen standard core samples were tested by X-ray diffraction (XRD), routine core analysis (RCA), and nuclear magnetic resonance (NMR) experiments. Moreover, five typical samples selected from the previous fifteen standard core samples were tested by the focused-ion-beam (FIB) experiment.

Detailed mineralogical and physical parameters of the fifteen samples are presented in Table 1. The results of the XRD analysis show a wide range of mineral compositions, which are dominated by carbonate and clay minerals. The dolomite contents are between 17.4% and 33.7% with an average of 26.2% (SD = 4.9%). The calcite contents range from 6.4% to 17.9%, with an average of 11.8% (SD = 3.3%). The clay contents range from 17.8% to 44.2% with an average of 30.1% (SD = 7.2%). In addition, the mineral compositions contain a moderate amount of quartz (an average = 15.2% and SD = 4.7%) and feldspar (an average = 11.1% and SD = 3.0%), and a low abundance of gypsum and pyrite. For the physical properties of the fifteen samples, the porosity and permeability vary from 1.53% to 12.65% (an average = 7.98% and SD = 3.68%), and 0.006 mD to 0.043 mD (an average = 0.024 mD and SD = 0.011 mD), respectively (Table 1).

2.2. Experiments. A large NMR analyzer (MacroMR12-150H-I) was used to test the fifteen core samples. The NMR experiment provides a waiting time of 3000 ms, echo spacing T_e 0.6 ms, and signal superposition times of 64 ms. The fifteen samples were firstly evacuated (-0.1 MPa) for 12 hours and then saturated with 100% water. Under the water-saturated (100%) condition, the fifteen samples had been NMR tested for the first time. Then, the HR2500-2 centrifugal machine was used to remove the movable water of the saturated samples under 600 psi centrifugal force. The fifteen samples were also had been tested by the NMR experiment for the second time after centrifugation. Finally, the incremental and cumulative T_2 spectrum distributions under water-saturated and irreducible conditions of the fifteen samples were obtained [7, 18, 31]. Moreover, the T_2 geometric mean (T_{2lm}), T_{35} , and T_{50} (the T_2 values corresponding to 35% and 50% saturation of the accumulated T_2 distribution curve, respectively) were also obtained by the T_2 spectra under water-saturated condition (Figure 1) [26, 35, 36].

TABLE 1: Correlation statistics of the minerals and the physical properties of the E_3^2 formation in the Yingxi area.

Sample no. & parameter	Helium porosity (%)	Helium permeability (mD)	Mineral compositions (%)						
			Dolomite	Calcite	Quartz	Feldspar	Clay	Gypsum	Pyrite
1	12.65	0.022	27.8	12.9	15.4	9.2	33.3	1.1	0.3
2	12.53	0.024	24.1	11.0	13.5	10.9	33.8	5.7	1.0
3	7.26	0.007	18.5	17.9	10.3	9.5	38.8	2.9	2.1
4	9.54	0.013	25.4	12.8	13.3	10.1	35.3	2.6	0.5
5	3.48	0.026	28.4	8.6	12.3	12.4	30.1	5.5	2.7
6	11.19	0.028	24.3	12.6	24.1	8.1	20.1	6.9	3.9
7	11.73	0.039	31.7	6.4	23.8	7.9	21.0	8.7	0.5
8	7.24	0.031	28.2	8.2	10.3	14.5	30.5	7.4	0.9
9	8.55	0.006	18.5	14.7	8.7	11.0	44.2	1.4	1.5
10	3.89	0.043	33.7	8.0	21.1	14.1	17.8	3.9	1.4
11	11.35	0.021	17.4	15.9	14.8	11.3	31.3	7.1	2.2
12	2.69	0.027	24.5	15.3	20.3	7.7	27.5	3.4	1.3
13	8.92	0.016	30.4	7.7	14.8	7.1	36.7	2.7	0.6
14	7.27	0.037	31.6	11.6	11.7	16.6	27.7	0.6	0.2
15	1.53	0.031	28.9	12.9	13.8	16.8	22.1	2.4	3.1
Average	7.98	0.024	26.2	11.8	15.2	11.1	30.1	4.2	1.5
SD	3.68	0.011	4.9	3.3	4.7	3.0	7.2	2.5	1.1

Note: SD: standard deviation.

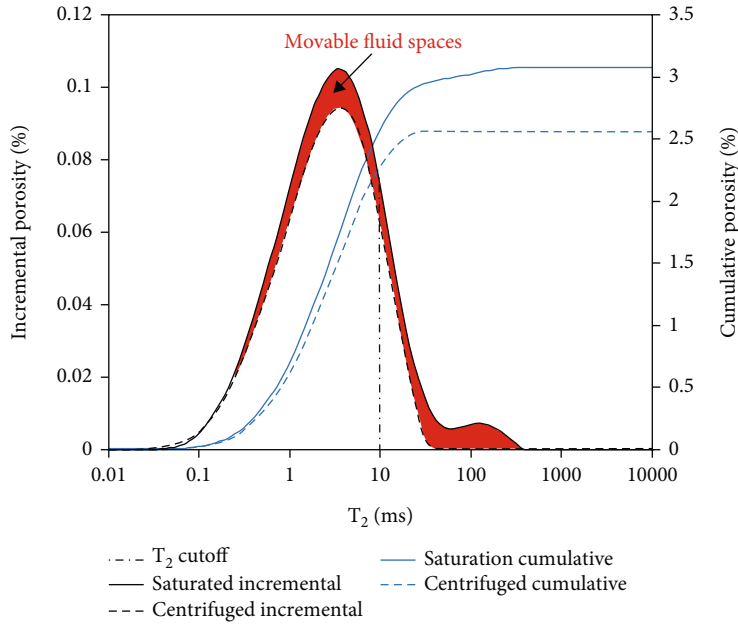


FIGURE 1: NMR T_2 distributions of the movable fluid space of the E_3^2 shales in the Yingxi area.

RCA experiment was performed on the fifteen samples using an automated CMM150/70-A under a net confining pressure of 10 MPa and a pore pressure of 7 MPa. Then, five core samples were selected for FIB testing with an accuracy of 10 nm. The maximum sphere algorithm was used to extract the pore-to-throat network models corresponding to the pore space topology of real cores, and the pore radii and throat radii in the three-dimensional

(3D) space were obtained. At last, the XRD experiment was applied to the fifteen samples. The fifteen samples were firstly powdered to less than $5 \mu\text{m}$, and then, the powder was followed at 90°C for 12 hours. A Bruker D8 Advance X-ray diffractometer was used to scan the powder of samples from 2° to 70° with a count time of 2 sec per 0.02° step [12]. Then, the TOPAS software was used to quantify the mineral contents.

2.3. Multifractal Methods. The characteristics of fractal sets can be described by the multifractal theory. Zhang et al. and Li et al. [23, 25] have particularly introduced detailed information on the multifractal theory. In this study, the box-counting method is applied to the multifractal analysis of the NMR T_2 distributions. Based on the dyadic scaling down method, the interval is partitioned as $J = [a, b]$ [20, 21, 25, 37]. The number of boxes $N(\varepsilon)$ of J at each scale size ε [$\varepsilon = (b - a) \cdot 2^{-k}$, k is a positive integer] is given by

$$N(\varepsilon) = 2^k. \quad (1)$$

In the rock, the probability measure $P_i(\varepsilon)$ of pore volume in the i th box is given by

$$P(\varepsilon) = \frac{N_i(\varepsilon)}{N(\varepsilon)}, \quad (2)$$

where the pore volume in the i th ($i = 1, 2, 3, \dots$) box is $N_i(\varepsilon)$ and the total volume of the rock is $N(\varepsilon)$.

$P_i(\varepsilon)$ has the following relationship with scale ε in a multifractal measure [38, 39]:

$$P_i(\varepsilon) = \varepsilon^{\alpha_i}, \quad (3)$$

where α_i is the singularity exponent corresponding to the singularity strength in the i th box, which describes the degree of nonuniformity of the probability subset.

When a singularity exponent increases $d\alpha$, the number of boxes is denoted as $N_\alpha(\varepsilon)$, and $N_\alpha(\varepsilon)$ increases as ε decreases [39]. Therefore, $N_\alpha(\varepsilon)$ can be given as follows:

$$N_\alpha(\varepsilon) \propto \varepsilon^{-f(\alpha)}, \quad (4)$$

where $f(\alpha)$ is a set of singularity spectrums with the same value of α [20], and the plot of $f(\alpha)$ versus α is known as the multifractal spectrum [20, 24].

For the multifractal spectrum, $f(\alpha)$ is generally a unimodal convex curve. The α and $f(\alpha)$ values can also be obtained from the following direct algorithms:

$$\begin{aligned} \alpha(q) &\propto \frac{\sum_{i=1}^{N(\varepsilon)} u_i(q, \varepsilon) \lg [P_i(\varepsilon)]}{\lg(\varepsilon)}, \\ f[\alpha(q)] &\propto \frac{\sum_{i=1}^{N(\varepsilon)} u_i(q, \varepsilon) \lg [u_i(q, \varepsilon)]}{\lg(\varepsilon)}, \end{aligned} \quad (5)$$

where q is the order of the statistical moment ($-\infty < q < +\infty$) and $N(\varepsilon)$ is the number of boxes of size ε [20, 24]. In addition, $\mu_i(q, \varepsilon)$ is a series of probability measures, which is defined as follows:

$$u_i(q, \varepsilon) = \frac{p_i^q(\varepsilon)}{\sum_{i=1}^{N(\varepsilon)} p_i^q(\varepsilon)}. \quad (6)$$

For the E_3^2 shales, the measures reflect the characteristics of pore size distributions [20, 39]. In order to ensure

that there is an excellent linear correlation between the $\mu_i(q, \varepsilon)$ and the scale size ε (correlation coefficient $\geq 90\%$), q is in the range from -10 to 10 in this study. α_{\min} and α_{\max} of the singularity exponents correspond to the $q = -10$ and of $q = 10$, respectively. α_0 of the singularity exponent corresponds to the peak of $f(\alpha)$ [20, 23, 39, 40]. In addition, many studies have shown that the left branch ($\alpha_0 - \alpha_{\max}$) with a larger width reflects the high probability measure and has a stronger heterogeneity, and the right branch ($\alpha_{\min} - \alpha_0$) with a larger width reflects the low probability measure and has a stronger heterogeneity [20, 23, 26, 36, 38].

3. Results

3.1. NMR T_2 Spectra of Movable Fluid Space and Total Pore Space. In the NMR experiment, the T_2 spectrum under water-saturated condition can reflect the pore size distribution of the total pore space [6, 30, 41]. After centrifugal, there is only irreducible water in the rocks, so the corresponding T_2 spectrum can reflect the pore size distribution of irreducible fluid space. Generally, T_2 cutoff (T_{2C}) is a relaxation time threshold that divides the total pore space into irreducible fluid space and the movable fluid space, whereas to the left of T_{2C} is irreducible water, and to the right of T_{2C} is movable water [6, 30, 42, 43]. However, it should be noted that the centrifuged curve is not zero even to the right of the T_{2C} ($T_2 > T_{2C}$) (Figure 1), implying that some portions considered movable water traditionally in the larger pores are not effectively movable [7, 44]. Meanwhile, the centrifuged T_2 curve to the left of the T_{2C} ($T_2 < T_{2C}$) is lower than the saturated T_2 curve (Figure 1), indicating that some portions considered irreducible water traditionally even in the smaller pores are also movable, which should be accounted as the movable water [6, 31]. Some similar phenomena can also be found in previous studies [20, 30, 31]. Thus, determining the distribution of the movable fluid space based on the T_2C needs better constraints. Actually, the movable fluid space from the NMR experiment should be the red shadow in Figure 1, i.e., the interval enclosed area by the T_2 spectrum curves under water-saturated and irreducible conditions.

The NMR characteristic parameters of the fifteen samples are listed in Table 2. As shown in Figure 2, there are three types of T_2 spectra for the E_3^2 shales: unimodal, isolated bimodal, and uninterrupted bimodal. The T_2 spectrum shapes of the movable fluid space are similar to that of the corresponding total pore space, and the T_2 peaks of the total pore space and movable fluid space are mainly distributed around 5 ms and 10 ms, respectively (Figure 2). However, there is more percentage of short T_2 distributions of the total pore space compared with that of the movable fluid space. Consequently, the total pore space has greater widths of the short T_2 distributions than that of the movable fluid space (Figure 2). In addition, it is worth noting that the three types of the T_2 spectra have significant differences in the total pore space, where the isolated bimodal and uninterrupted bimodal types all distinctly have a few long T_2 distributions compared with the unimodal type (Figures 2(a)–2(c)). The same applies to the movable fluid space (Figures 2(d)–2(f)).

TABLE 2: Correlation statistics of the NMR parameters and the multifractal parameters of the E_3^2 shales in the Yingxi area.

Sample no.	NMR and multifractal parameters				
	T_{35} (ms)	T_{50} (ms)	T_{2lm} (ms)	$[\alpha(x)_0 - \alpha(x)_{max}]$	$[\alpha(y)_0 - \alpha(y)_{max}]$
1	0.74	3.33	2.12	0.79	0.24
2	1.28	4.51	3.12	0.71	0.25
3	0.76	3.59	2.37	0.83	0.27
4	1.04	3.55	2.69	0.77	0.23
5	1.58	5.88	2.65	0.64	0.22
6	3.06	7.14	4.84	0.47	0.15
7	3.24	6.89	4.64	0.55	0.12
8	1.42	4.58	2.29	0.73	0.19
9	0.64	3.18	1.34	0.87	0.32
10	5.08	8.12	5.83	0.45	0.09
11	1.87	5.01	2.86	0.76	0.21
12	2.34	4.15	3.19	0.64	0.20
13	0.98	4.12	1.71	0.79	0.28
14	1.85	5.14	3.57	0.66	0.16
15	2.99	4.92	3.78	0.59	0.14
Average	1.92	4.94	3.13	0.68	0.20
SD	1.19	1.43	1.19	0.12	0.06

Note: SD: standard deviation.

3.2. NMR Multifractal Spectra. The multifractal spectra of NMR T_2 distributions of the total pore space and movable fluid space are shown in Figure 3, and the characteristic parameters of the multifractal spectra are listed in Table 2. For the corresponding multifractal spectra, the unimodal type of the T_2 spectra all have greater widths of the left branch than that of the isolated bimodal and uninterrupted bimodal types (Figure 3). As mentioned in Section 3.1, there is more percentage of long T_2 distributions in the isolated bimodal and uninterrupted bimodal types compared with the unimodal type for the total pore space and the movable fluid space. Due to the widths of the left branch of multifractal spectra corresponding to the heterogeneity of the high probability measure areas of the T_2 distributions, the higher ($\alpha_0 - \alpha_{max}$) values reflect that the high probability measure areas have a stronger heterogeneity (Table 2 and Figure 3) [20, 21]. Thus, the heterogeneity of the high-probability measure areas is influenced by the percentage of the long T_2 distributions (Figures 2 and 3).

Additionally, the multifractal spectra of the T_2 distributions for the total pore space and movable fluid space are all right-skewed, but the widths of the left branch of the total pore space are greater than that of the movable fluid space (Figure 3). Correspondingly, the total pore space has more percentage of the short T_2 distributions than that of the movable fluid space. So the percentages of the short T_2 distributions also influence the heterogeneity of the high probability measure areas (Figures 2 and 3). However, there are no significant differences in the widths of the right branch of the multifractal spectra for the total pore space, and the same is true for the movable fluid space (Figure 3). Thus, it is appropriate to use the high probability measure areas to analyze the pore structure of the E_3^2 shales.

3.3. Pore Structure from 3D CT. Based on the XRD results (Table 1), samples 9, 11, 10, 12, and 15 were tested by the FIB experiment, and their 3D pore structures were reconstructed. It can be found that the pores and throats of the five samples are all in a relatively homogeneous dispersion state in the 3D space (Figures 4(a)–4(e)). Samples 10 and 15 are mainly composed of the silicate (quartz+feldspar) and carbonate minerals, and the main minerals of sample 12 are the silicate (quartz+feldspar), carbonate, and clay minerals, whereas samples 11 and 9 are mainly composed of the carbonate and clay minerals (Table 1). The pore types of samples 10, 15, and 12 are dominated by the intergranular pores of the quartz and feldspar minerals (Figures 4(f)–4(h)). In contrast, the intercrystalline pores of the dolomite, calcite, and clay minerals are widely developed in samples 11 and 9 (Figures 4(i) and 4(j)). In addition, it is worth noting that the radius distributions of the throats are closely related to the radius distributions of the interconnected pores in the same shale sample, and the larger the average pore radius is, the larger the average throat radius is (Figure 5). For example, samples 10, 15, and 12 all have a relatively high percentage of large pores. Their average pore radii and throat radii are 158 nm, 126 nm, and 89 nm and 144 nm, 101 nm, and 81 nm, respectively. In contrast, there is a high percentage of small pores and throats in samples 11 and 9, which only have average pore radii and throat radii of 47 nm and 33 nm and 32 nm and 26 nm, respectively (Figure 5).

Based on Table 1 and Figure 5, the radius distributions of pores and throats have significant relationships with the mineral contents of the E_3^2 shales. For example, samples 10, 15, and 12, which are dominated by the minerals of quartz and feldspar minerals, all have a high percentage of

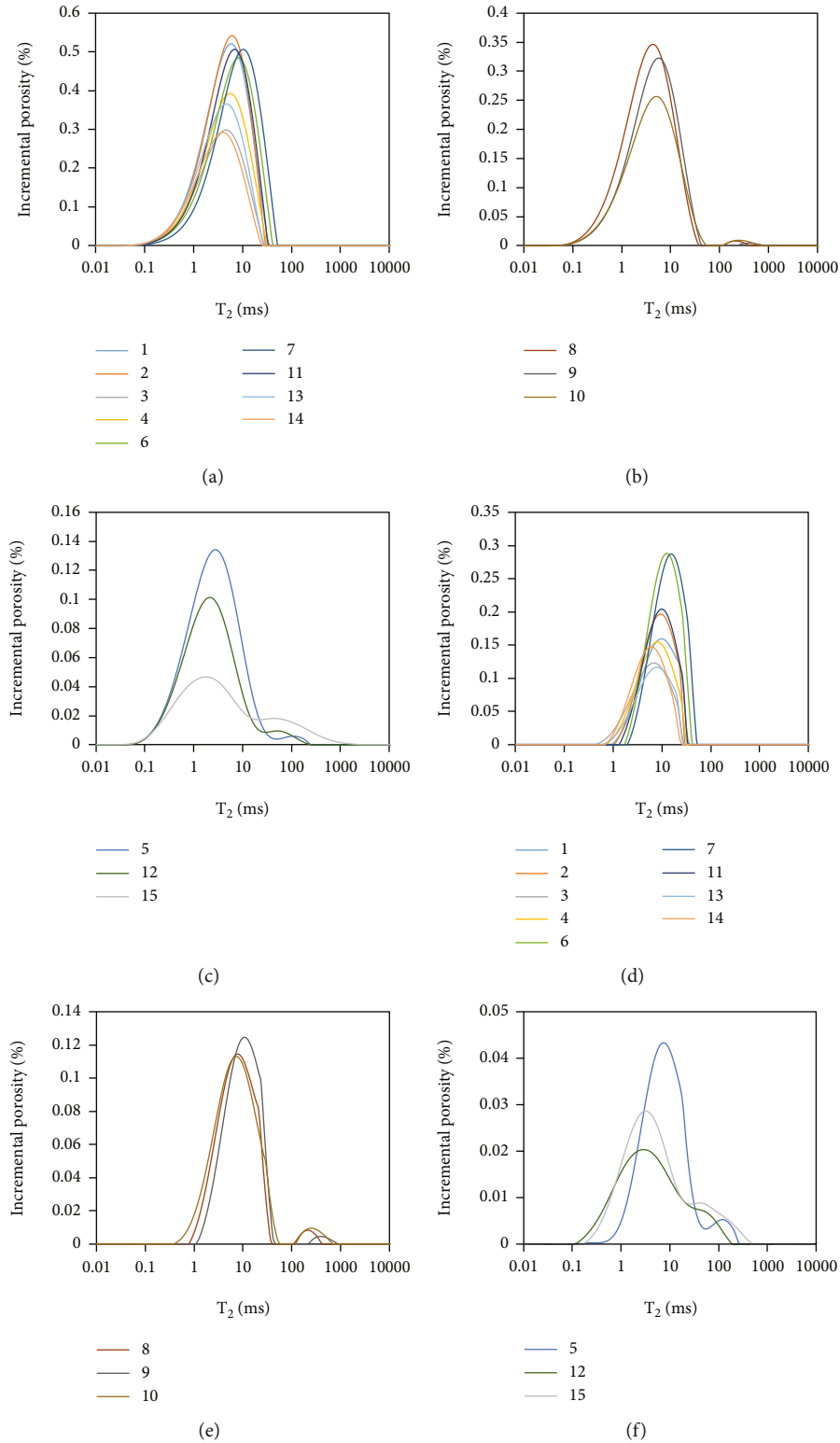


FIGURE 2: Characteristics of the T_2 distributions, (a) unimodal types of the total pore space, (b) isolated bimodal types of the total pore space, (c) uninterrupted bimodal types of the total pore space, (d) unimodal types of the movable fluid space, (e) isolated bimodal types of the movable fluid space, and (f) uninterrupted bimodal types of the movable fluid space.

large pores and throats, while there is a high percentage of small pores and throats in samples 11 and 12 with more clay minerals. Moreover, the average pore radius and throat

radius appreciably increase with the increasing contents of the (quartz+feldspar) minerals, but the high contents of clay minerals significantly negatively influence the average pore

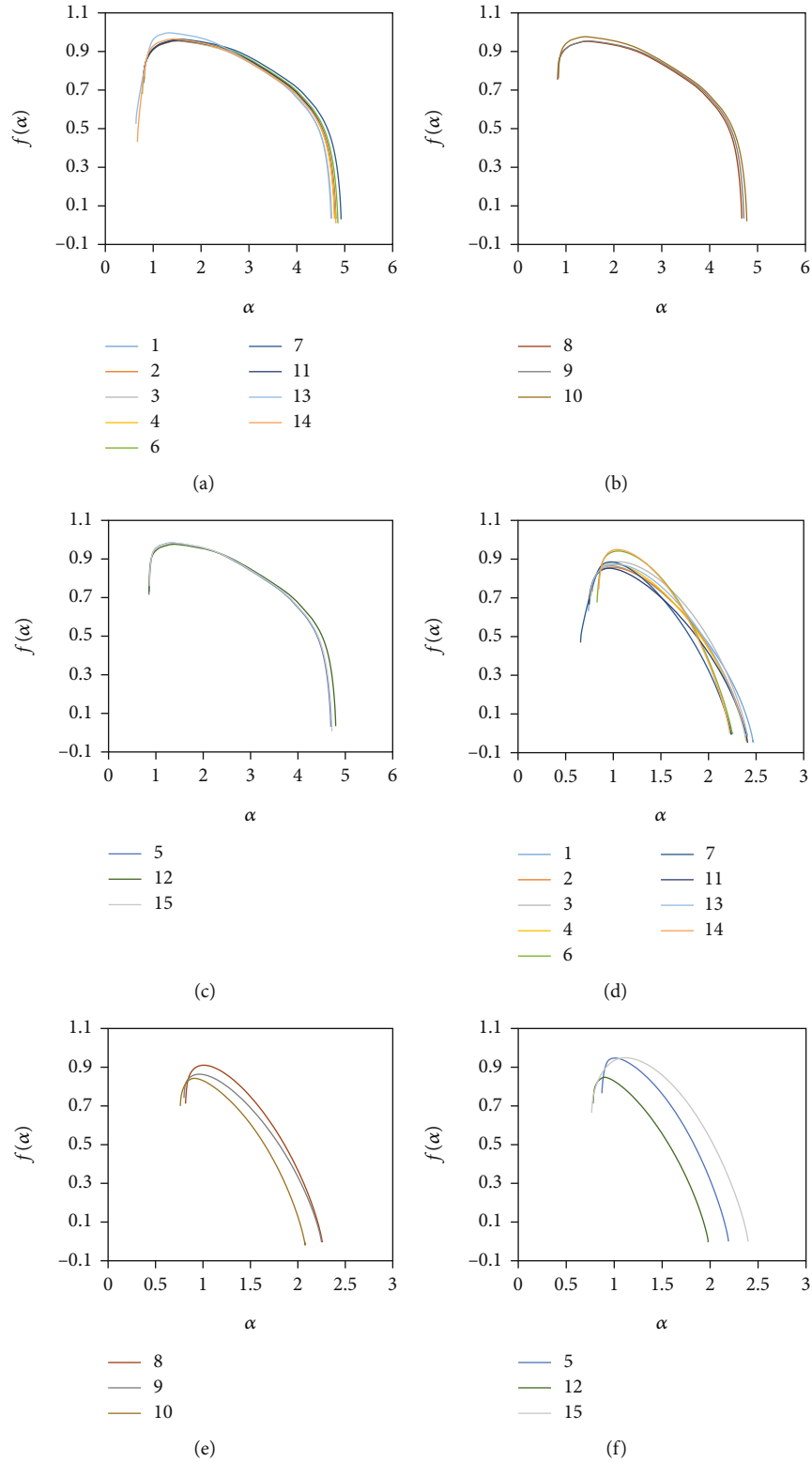


FIGURE 3: The relationships between the $f(\alpha)$ and α , i.e., multifractal spectra, (a) the unimodal types of T_2 spectra for the total pore space, (b) the isolated bimodal types of T_2 spectra for the total pore space, (c) the uninterrupted bimodal types of T_2 spectra for the total pore space, (d) the unimodal types of T_2 spectra for the movable fluid space, (e) the isolated bimodal types of T_2 spectra for the movable fluid space, and (f) the uninterrupted bimodal types of T_2 spectra for the movable fluid space.

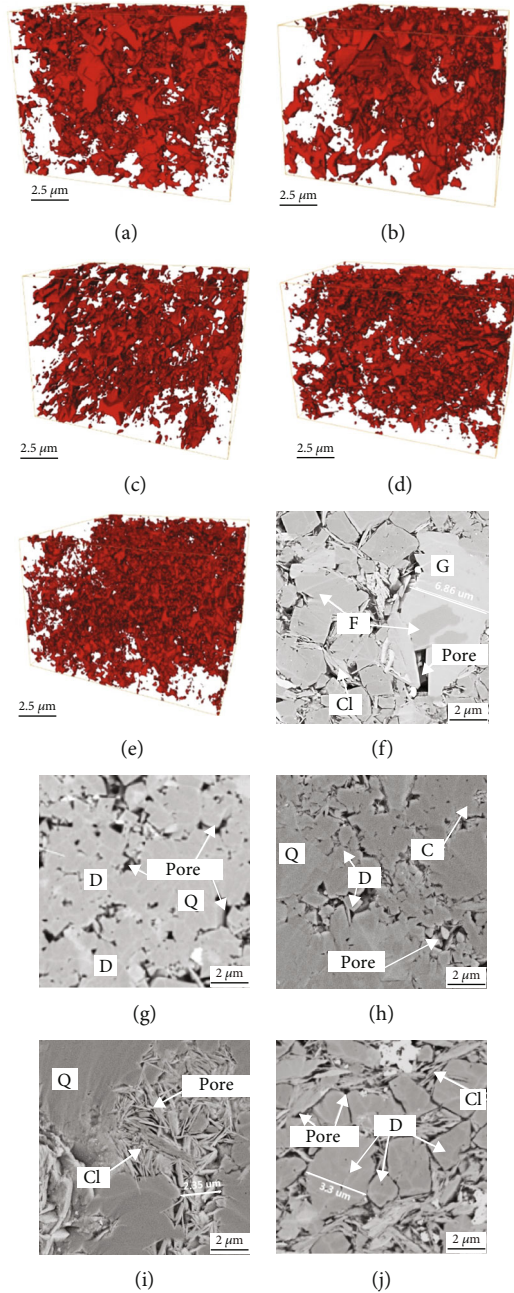


FIGURE 4: 3D pore structures and pore types of the typical E_3^2 shale samples in the Yingxi area. (a, f) Sample 10, (b, g) sample 15, (c, h) sample 12, (d, i) of sample 11, and (e, j) sample 9; (f, g) intergranular pores, (h) carbonate intercrystalline pores, and (i, j) clay intercrystalline pores. Note: D: dolomite; C: calcite; F: feldspar; Q: quartz; Cl: clay; G: gypsum.

radius average throat radius (Table 1 and Figure 5). These reveal that the clay, quartz, and feldspar minerals play essential roles in controlling pore structure characteristics for the E_3^2 shales.

4. Discussions

4.1. Relationships between Multifractal Parameters and NMR Parameters. The widths of the left branch of the multifractal spectra can reflect the characteristics of T_2 distributions obviously, and the $[\alpha(x)_0 - \alpha(x)_{\max}]$ and $[\alpha(y)_0 - \alpha(y)_{\max}]$ corre-

spond to the heterogeneity of the high probability measure areas of the total pore space and the movable pore space, respectively. As shown in Figures 6(a) and 6(b), the $[\alpha(x)_0 - \alpha(x)_{\max}]$ and $[\alpha(y)_0 - \alpha(y)_{\max}]$ all have strong negative correlations with the T_{2lm} . Owing to the T_{2lm} is mainly influenced by the long T_2 distributions, and the more percentage of the long T_2 distributions, the larger the T_{2lm} [26, 35, 36, 45]; thus, the lower values of the $[\alpha(x)_0 - \alpha(x)_{\max}]$ and $[\alpha(y)_0 - \alpha(y)_{\max}]$ correspond to the more percentage of long T_2 distributions, and the T_{2lm} decreases with the increasing of the $[\alpha(x)_0 - \alpha(x)_{\max}]$ and $[\alpha(y)_0 - \alpha(y)_{\max}]$. It is worth noting that the T_{2lm} has a

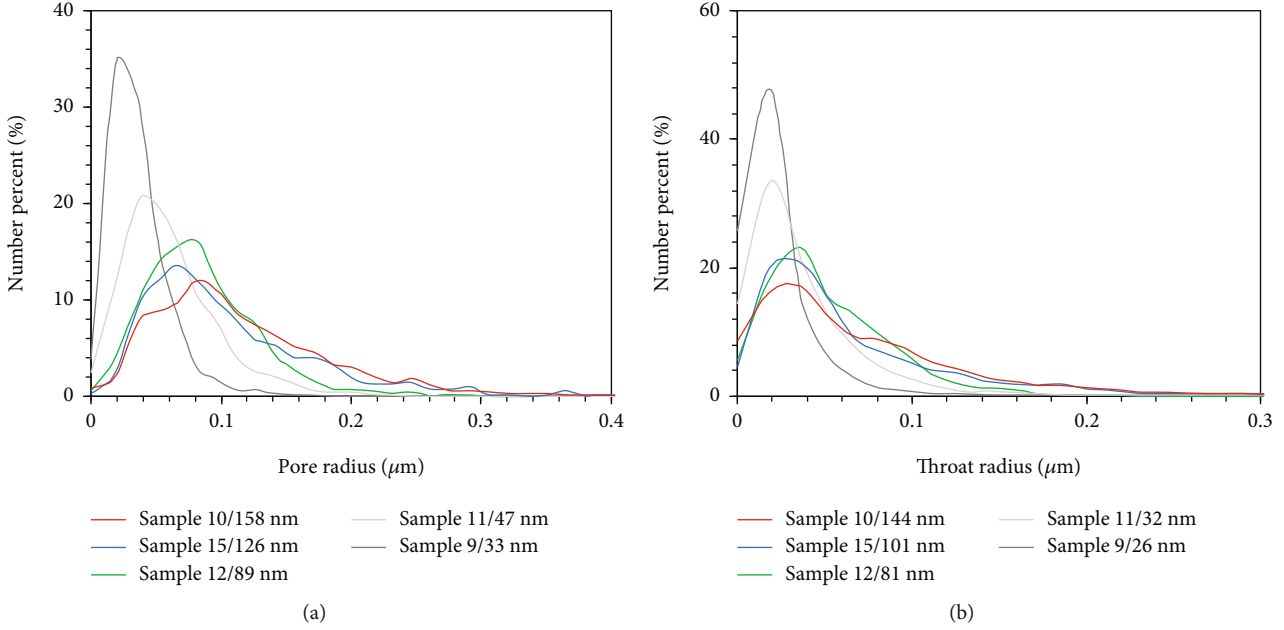


FIGURE 5: Radius distribution characteristics of pores (a) and throats (b) of the five E_3^2 shale samples, average value is after “/”.

better correlation with the $[\alpha(x)_0 - \alpha(x)_{\max}]$ than with the $[\alpha(y)_0 - \alpha(y)_{\max}]$. This may be due to the $T_{2\text{lm}}$ directly corresponding to the T_2 distributions of the total pore space. However, the T_2 distributions of the movable pore space cannot entirely reflect the actual T_2 distributions of the total pore space.

In the NMR experiment, the lower the T_{35} or the T_{50} is, the higher the percentage of the short T_2 distributions is [26, 35, 45]. Figures 6(c) and 6(d) show that the $[\alpha(x)_0 - \alpha(x)_{\max}]$ has a good negative correlation with the T_{50} , and there is a moderate negative correlation between the $[\alpha(y)_0 - \alpha(y)_{\max}]$ and T_{50} . Moreover, both the $[\alpha(x)_0 - \alpha(x)_{\max}]$ and $[\alpha(y)_0 - \alpha(y)_{\max}]$ decrease with the increase of the T_{35} and the correlation of the $[\alpha(y)_0 - \alpha(y)_{\max}]$ with T_{35} is better than that of the $[\alpha(x)_0 - \alpha(x)_{\max}]$ with T_{35} (Figures 7(e) and 7(f)). These indicate that the $[\alpha(x)_0 - \alpha(x)_{\max}]$ and $[\alpha(y)_0 - \alpha(y)_{\max}]$ are more sensitive to the T_{50} and T_{35} , respectively. This may be because the total pore space has more percentage of short T_2 distributions than that of the movable pore space, as discussed in Section 3.1.

4.2. Relationships between Multifractal Parameters and Pore Structure Parameters. In order to understand the role of the pore structure on the multifractal characteristics in the E_3^2 shales, the correlated scatterplots between the pore structure parameters and the multifractal parameters are shown in Figure 7. The average pore radius has a strong negative correlation with the $[\alpha(x)_0 - \alpha(x)_{\max}]$ with a correlation coefficient of $R^2 = 0.931$ (Figure 7(a)), which is consistent with the studies of tight sandstone [20], fine dolomite [23], and fresh coal [24]. In contrast, the average pore radius shows a general negative correlation with the $[\alpha(y)_0 - \alpha(y)_{\max}]$ (Figure 7(b)), which means the average pore radius has a significant impact on the $[\alpha(x)_0 - \alpha(x)_{\max}]$ instead of the $[\alpha$

$(y)_0 - \alpha(y)_{\max}]$. This may be because the movable pore space is only a fraction of the total pore space and cannot represent the distribution of all pores. As discussed in Section 3.4.2, the higher values of the $[\alpha(x)_0 - \alpha(x)_{\max}]$ and $[\alpha(y)_0 - \alpha(y)_{\max}]$ correspond to the more percentage of the short T_2 distributions in the T_2 spectra. Meanwhile, the T_2 values correspond to the different pore sizes of rocks in the NMR experiment [7, 30, 31]. Thus, the E_3^2 shales with lower $[\alpha(x)_0 - \alpha(x)_{\max}]$ and $[\alpha(y)_0 - \alpha(y)_{\max}]$ may have less percentage of small pores, which leads to a good pore structure with a larger average pore radius.

The average throat radius has different correlations with the $[\alpha(x)_0 - \alpha(x)_{\max}]$ and $[\alpha(y)_0 - \alpha(y)_{\max}]$. There is a general negative correlation between the average throat radius and the $[\alpha(x)_0 - \alpha(x)_{\max}]$ (Figure 7(c)). Instead, the $[\alpha(y)_0 - \alpha(y)_{\max}]$ has a strong negative correlation with the average throat radius (Figure 7(d)). These findings suggest that the $[\alpha(y)_0 - \alpha(y)_{\max}]$ can effectively represent the average throat radius of the E_3^2 shales. Generally, the throat radius is always smaller than the corresponding connected pore radius in rocks [6, 46, 47], so the short T_2 distributions may best represent the distribution of throat radius. Thus, the $[\alpha(y)_0 - \alpha(y)_{\max}]$ is more sensitive to the average throat radius because the T_{35} has a better correlation with the $[\alpha(y)_0 - \alpha(y)_{\max}]$ than that of the $[\alpha(x)_0 - \alpha(x)_{\max}]$. Moreover, the E_3^2 shales with higher $[\alpha(y)_0 - \alpha(y)_{\max}]$ may have a larger average throat radius, which is in favor of the fluids flow.

4.3. Effects of Shale Compositions on Multifractal Parameters. Mineral compositions of the E_3^2 shales are particularly complex and have an essential control on the pore structure [7, 45, 46]. Meanwhile, there are clear connections between the pore structure parameters and multifractal parameters, so it is also necessary to discuss the effects of mineral

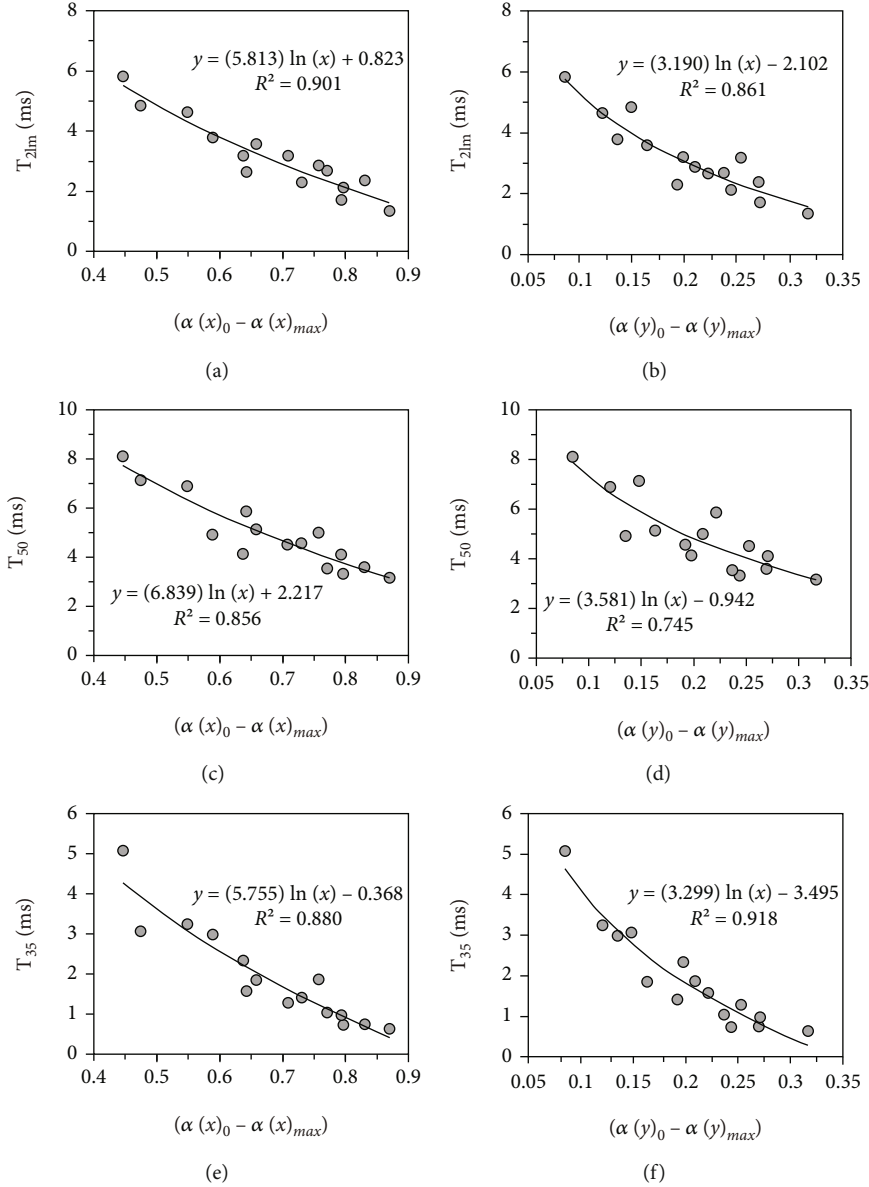


FIGURE 6: Relationships between the multifractal parameters and the NMR parameters. (a, b) The comparison of the relationship between the T_{2lm} and the multifractal parameters, (c, d) the comparison of the relationship between the T_{50} and the multifractal parameters, and (e, f) the comparison of the relationship between the T_{35} and the multifractal parameters.

compositions on the multifractal characteristics. As shown in Figures 8(a) and 8(b), the (quartz+feldspar) contents have moderate and strong negative correlations with the $[\alpha(x)_0 - \alpha(x)_{max}]$ and $[\alpha(y)_0 - \alpha(y)_{max}]$, respectively. The E_3^2 shales with higher contents of (quartz+feldspar) minerals generally have larger radii of pores and throats, which is because the intergranular pores developed in the quartz and feldspar minerals are mostly protected by the brittle minerals and thus, producing more macropores easily (Figures 4(f) and 4(g)). Due to the average pore radius increases with the increasing percentage of the macropores in the rocks [7, 45, 46, 48], thus, the contents of (quartz+feldspar) minerals in the E_3^2 shales may influence the pores radii, and in turn, impact on the multifractal parameters. Moreover, the

contents of (quartz+feldspar) minerals have a better correlation with the $[\alpha(y)_0 - \alpha(y)_{max}]$ than that with the $[\alpha(x)_0 - \alpha(x)_{max}]$, which may be the movable fluid space is dominated by the macropores developed in the (quartz+feldspar) minerals. Therefore, the E_3^2 shales with a high content of (quartz+feldspar) minerals tend to have a good pore structure.

Figures 8(c) and 8(d) show that both the $[\alpha(x)_0 - \alpha(x)_{max}]$ and $[\alpha(y)_0 - \alpha(y)_{max}]$ have strong positive correlations with the contents of clay minerals, indicating the content of clay minerals in the E_3^2 shales is the main factor controlling the pore structure. This may be because the content of clay minerals plays a vital role in decreasing the pore and throat radius. As shown in Figures 4(i) and 4(j), the clay minerals are prone to deformation during the compaction

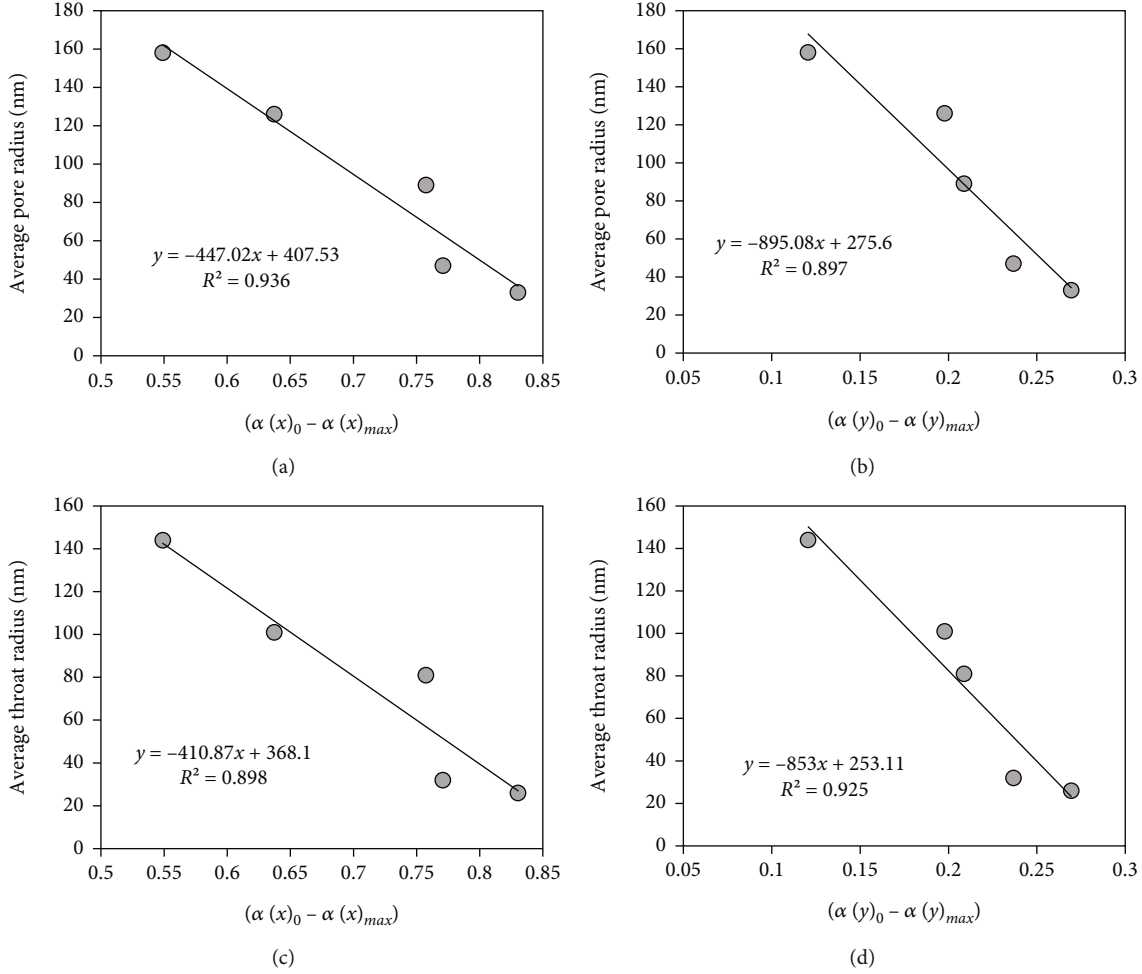


FIGURE 7: Relationships between the (a, b) average pore radius, (c, d) average throat radius, and the multifractal parameters.

process, leading to the clay intercrystalline pores collapsing without protection, and thus producing more micropores in the E_3^2 shales [48, 49]. Additionally, at higher clay minerals levels of the E_3^2 shales, the intergranular pores supported by the brittle minerals are easily filled with fine impurities of the clay minerals, consequently resulting in a further reduction in pore spaces (Figure 4(j)). Therefore, the higher content of the clay minerals is not conducive to the formation of a good pore structure in the E_3^2 shales. In addition, the contents of carbonate minerals have slight negative correlations with the $[\alpha(x)_0 - \alpha(x)_{max}]$ and $[\alpha(y)_0 - \alpha(y)_{max}]$ (Figures 8(e) and 8(f)), which means the carbonate minerals are also conducive to the formation of a good pore structure but with less effect on the pore structure compared with the (quartz+feldspar) minerals. This may depend on whether the intercrystalline carbonate pores are filled with the clay minerals or protected by the quartz and feldspar minerals during the diagenesis of the E_3^2 shales [43, 48], while the real reason needs to be further explored.

4.4. Multifractal Model for Permeability Estimation. Permeability estimation has always been the key to evaluate shale reservoirs [24, 35, 44, 47]. However, it is a problem to estimate the permeability accurately by the well-logging

method. As discussed in Section 4.2, the average pore radius and average throat radius have strong negative correlations with the $[\alpha(x)_0 - \alpha(x)_{max}]$ and $[\alpha(y)_0 - \alpha(y)_{max}]$, respectively, which provides a new way to estimate the permeability in core scale and well-logging scale. Obviously, the $[\alpha(x)_0 - \alpha(x)_{max}]$ can be obtained by the T_2 spectra under water-saturated condition, while the $[\alpha(y)_0 - \alpha(y)_{max}]$ must be obtained by using the T_2 spectra under water-saturated and irreducible conditions. For core samples, the $[\alpha(x)_0 - \alpha(x)_{max}]$ and $[\alpha(y)_0 - \alpha(y)_{max}]$ can be applied to estimate the permeability. After multiple linear regression calculations, the permeability K can be expressed as

$$K = 0.0704 - 0.0365[\alpha(x)_0 - \alpha(x)_{max}] - 0.1102[\alpha(y)_0 - \alpha(y)_{max}]. \quad (7)$$

However, Equation (7) cannot be applied in the well logging to estimate the permeability because the $[\alpha(y)_0 - \alpha(y)_{max}]$ cannot be obtained by the NMR well logging. As discussed in Section 4.1, the $[\alpha(y)_0 - \alpha(y)_{max}]$ has good correlations with the T_{2lm} and T_{35} ; meanwhile, the T_{2lm} and T_{35} can be obtained by the NMR well logging. Thus, the $[\alpha(x)_0 - \alpha(x)_{max}]$, T_{2lm} , and T_{35} can be used to estimate the

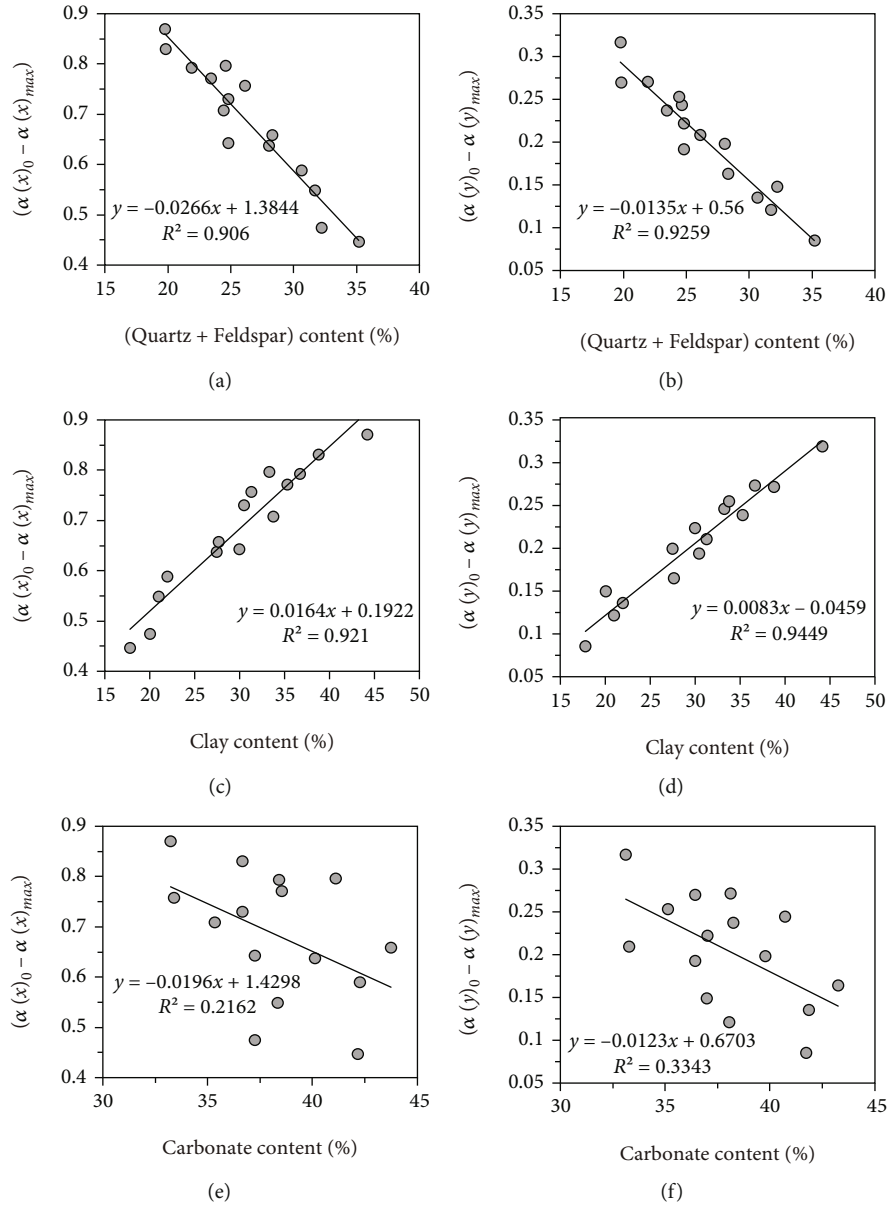


FIGURE 8: Relationships between the shale composition and the multifractal parameters. (a, b) The comparison of the relationship between the (quartz+feldspar) content and the multifractal parameters, (c, d) the comparison of the relationship between the clay content and the multifractal parameters, and (e, f) the comparison of the relationship between the carbonate content and the multifractal parameters.

permeability in the NMR well logging. After multiple linear regression calculations, the permeability obtained by the NMR well logging can be given as

$$K = 0.0496 + 0.0031 \times T_{35} + 0.0009 \times T_{2lm} - 0.0516 [\alpha(x)_0 - \alpha(x)_{\max}] \quad (8)$$

In order to verify the accuracy of Equations (7) and (8), the estimated permeability is compared with the Helium permeability of the new ten samples from the E_3^2 shales. Figure 9 shows that all the estimated data points fall approximately on the intersection lines, which means the permeability values calculated by the multifractal models agree well with the measured results. Overall, the $[\alpha(x)_0 - \alpha(x)_{\max}]$ and $[\alpha(y)_0 -$

$\alpha(y)_{\max}]$ are the primary influence factors of permeability for the E_3^2 shales. For the E_3^2 shales, the pores are dominated by small sizes and concentrated in a narrow range. Previous studies have shown that the small pores are highly irregular in shape, and many small pores will enhance the heterogeneity of pore spaces [16, 21, 48, 50]. Meanwhile, the higher $[\alpha(x)_0 - \alpha(x)_{\max}]$ or $[\alpha(y)_0 - \alpha(y)_{\max}]$ represent that the E_3^2 shales have more percentage of small pores within a narrow range. Thus, the permeability decreases with the increase of $[\alpha(x)_0 - \alpha(x)_{\max}]$ and $[\alpha(y)_0 - \alpha(y)_{\max}]$. Notably, the Helium permeability has a better negative correlation with the $[\alpha(y)_0 - \alpha(y)_{\max}]$ than that of it with the $[\alpha(x)_0 - \alpha(x)_{\max}]$ (Figure 9), indicating that the permeability is significantly influenced by the heterogeneity of the movable fluid space.

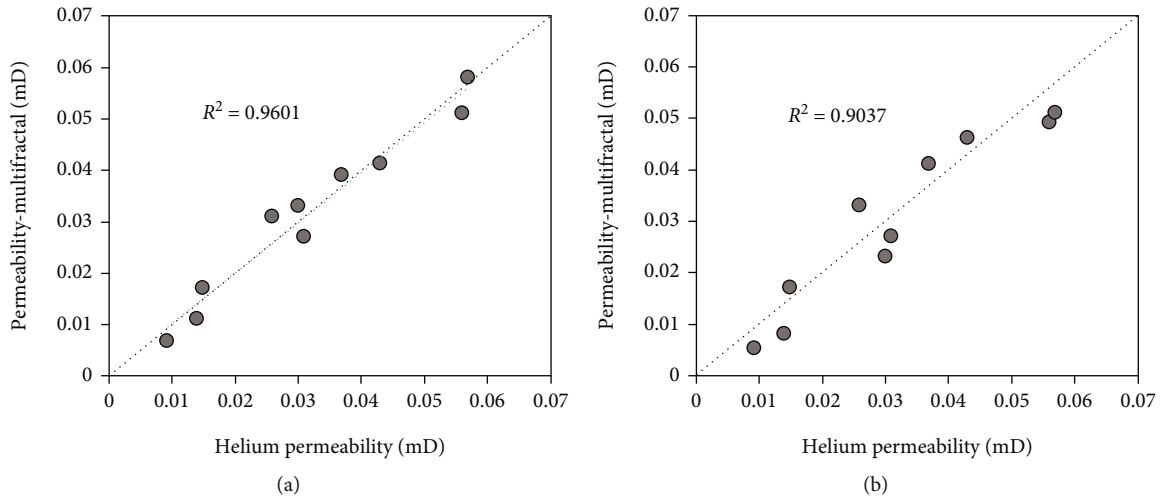


FIGURE 9: Cross plots of the Helium permeability vs. the permeability obtained by (a) Equation (7) and (b) Equation (8).

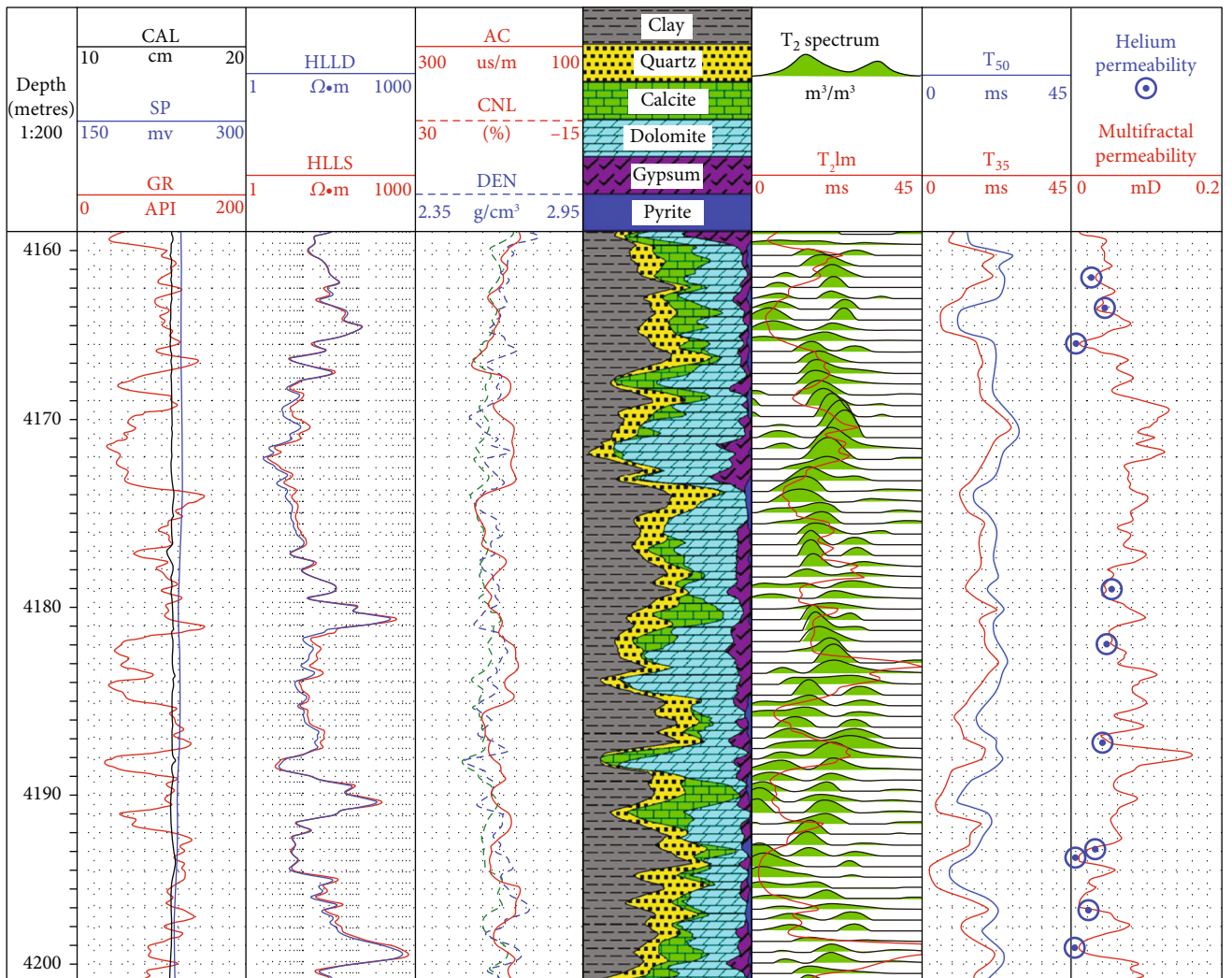


FIGURE 10: The permeability results estimated from the NMR well logging for the E₃² shales. Note: gamma-ray logs (GR), caliper logs (CAL), compensated neutron logs (CNL), density logs (DEN), acoustic logs (AC), self-potential (SP), deep lateral logging resistivity (HLLD), short lateral logging resistivity (HLLS), T₂ spectrum obtained by NMR well logs.

As shown in Figure 10, the NMR T_2 distributions are presented in the fourth track, both the T_{35} and T_{2lm} are presented in the fifth track, the sixth track includes the left branch widths of the multifractal spectra $[\alpha(x)_0 - \alpha(x)_{max}]$, the seventh track includes the permeability calculated by Equation (8) and the Helium permeability, and the eighth track includes the mineral contents obtained by the elemental capture spectroscopy (ECS) log. The results of the permeability calculated by Equation (8) agree well with the Helium permeability and mineral contents, respectively. Thus, the proposed multifractal models can be effective methods to estimate the permeability of the E_3^2 shales both in the core scale and the well-logging scale. In addition, it is worth noting that previous statistical models for the permeability estimation are useful only for certain reservoirs because they always depend on the correlation coefficients between the permeability and the radii of the pores or throats, whereas the proposed multifractal models for the permeability estimation does not need these, and thus the proposed multifractal methods in this study are convenient and applicable for the other reservoirs.

5. Conclusions

- (1) The current method of determining the movable fluid space based on the T_2 cutoff has its limitation, whereas using the interval enclosed area by the T_2 spectrum curves under water-saturated and irreducible conditions is more accurate. For the E_3^2 shales, the T_2 distributions of the total pore space have stronger high probability measure areas than that of the movable fluid space, and using the high probability measure areas of the T_2 distributions to characterize the multifractal characteristics of the pore structure is more appropriate
- (2) The T_{2lm} , T_{50} , and T_{35} all decrease with the increase of the $[\alpha(x)_0 - \alpha(x)_{max}]$ and $[\alpha(y)_0 - \alpha(y)_{max}]$, indicating that the lower $[\alpha(x)_0 - \alpha(x)_{max}]$ and $[\alpha(y)_0 - \alpha(y)_{max}]$ are associated with the more percentage of large pores in the E_3^2 shales. Meanwhile, the average radii of pore and throat decrease with an increase in the $[\alpha(x)_0 - \alpha(x)_{max}]$ and $[\alpha(y)_0 - \alpha(y)_{max}]$, suggesting that the E_3^2 shales with lower $[\alpha(x)_0 - \alpha(x)_{max}]$ and $[\alpha(y)_0 - \alpha(y)_{max}]$ may have a good pore structure
- (3) The mineral compositions have different effects on the pore structure of the E_3^2 shales, which in turn exert influences on the multifractal parameters. As the (quartz+feldspar) mineral content increases, the large pore content increases; in contrast, a higher clay mineral content leads to a smaller average pore size. Thus, the high (quartz+feldspar) mineral content plays a positive role in generating low $[\alpha(x)_0 - \alpha(x)_{max}]$ and $[\alpha(y)_0 - \alpha(y)_{max}]$, while an increase in the clay mineral content increases the $[\alpha(x)_0 - \alpha(x)_{max}]$ and $[\alpha(y)_0 - \alpha(y)_{max}]$
- (4) For the E_3^2 shale reservoirs, a new multifractal model in core scale was provided for estimating permeability based on the multifractal parameters of $[\alpha(x)_0 - \alpha(x)_{max}]$ and $[\alpha(y)_0 - \alpha(y)_{max}]$. Moreover, the T_{2lm} , T_{35} , and $[\alpha(x)_0 - \alpha(x)_{max}]$ were used to establish a novel permeability model in NMR well-logging scale, which is independent of any help from any other core experiments. Overall, the provided models for permeability estimation of the E_3^2 shales in core scale and well-logging scale are convenient and accurate, which are also applicable for the other reservoirs

Data Availability

The core test data and log data used to support the findings of this study have not been made available because of the unit for data confidentiality requirements.

Conflicts of Interest

The authors declare that they have no conflicts of interest.

Acknowledgments

This work was financially supported by the Project of Science and Technology Department of Sinopec (P21075-1, P21075-2, and P22213-4), the China Postdoctoral Science Foundation (2022M723499), and the National Natural Science Foundation of China (41872133).

References

- [1] D. Palermo, T. Aigner, M. Geluk, M. Poppelreiter, and K. Pipping, "Reservoir potential of a lacustrine mixed carbonate/siliciclastic gas reservoir: the Lower Triassic Rogenstein in the Netherlands," *Journal of Petroleum Geology*, vol. 31, no. 1, pp. 61–96, 2008.
- [2] K. M. Bohacs, A. R. Carroll, J. E. Neal, and P. J. Mankiewicz, "Lake-basin type, source potential, and hydrocarbon character: an integrated-sequence-stratigraphic-geochemical framework," *AAPG Bulletin*, vol. 46, pp. 3–34, 2000.
- [3] L. Caracciolo, P. Gramigna, S. Critelli, A. B. Calzona, and F. Russo, "Petrostratigraphic analysis of a Late Miocene mixed siliciclastic-carbonate depositional system (Calabria, Southern Italy): implications for Mediterranean paleogeography," *Sedimentary Geology*, vol. 284–285, pp. 117–132, 2013.
- [4] J. G. Wang, D. W. Zhang, S. Y. Yang et al., "Sedimentary characteristics and genesis of the salt lake with the upper member of the Lower Ganchaigou Formation from Yingxi sag, Qaidam basin," *Marine and Petroleum Geology*, vol. 111, pp. 135–155, 2019.
- [5] R. G. Loucks, R. M. Reed, S. C. Ruppel, and D. M. Jarvie, "Morphology, genesis, and distribution of nanometer-scale pores in siliceous mudstones of the Mississippian Barnett Shale," *Journal of Sedimentary Research*, vol. 79, no. 12, pp. 848–861, 2009.
- [6] Q. Q. Dai, Q. Luo, C. Zhang et al., "Pore structure of tight sandstone oil reservoir based on new parameter from NMR: evidences from Chang 7 Member in Ordos Basin, China," *Acta Petrolei Sinica*, vol. 37, no. 7, pp. 887–897, 2016.

- [7] J. Lai, G. W. Wang, J. T. Cao et al., "Investigation of pore structure and petrophysical property in tight sandstones," *Marine and Petroleum Geology*, vol. 91, pp. 179–189, 2018.
- [8] D. Ross and R. M. Bustin, "The importance of shale composition and pore structure upon gas storage potential of shale gas reservoirs," *Marine and Petroleum Geology*, vol. 26, no. 6, pp. 916–927, 2009.
- [9] Y. Zhu, Y. Wang, S. Chen, H. Zhang, and F. U. Chang, "Qualitative-quantitative multiscale characterization of pore structures in shale reservoirs: a case study of Longmaxi formation in the Upper Yangtze area," *Earth Science Frontiers*, vol. 23, no. 1, pp. 154–163, 2016.
- [10] I. O. Yilmaz and D. Altın, "Cyclostratigraphy and sequence boundaries of inner platform mixed carbonate-siliciclastic successions (Barremian-Aptian) (Zonguldak, NW Turkey)," *Journal of Asian Earth Sciences*, vol. 30, no. 2, pp. 253–270, 2007.
- [11] D. Korngreen and O. M. Bialik, "The characteristics of carbonate system recovery during a relatively dry event in a mixed carbonate/siliciclastic environment in the Pelsonian (Middle Triassic) proximal marginal marine basins: a case study from the tropical Tethyan Northwest Gondwana margins," *Palaeogeography, Palaeoclimatology, Palaeoecology*, vol. 440, pp. 793–812, 2015.
- [12] A. Furmann, M. Mastalerz, D. Bish, A. Schimmelmann, and P. Pedersen, "Porosity and pore size distribution in mudrocks from the Belle Fourche and Second White Specks Formations in Alberta, Canada," *AAPG Bulletin*, vol. 100, no. 8, pp. 1265–1288, 2016.
- [13] X. Niu, D. Yan, M. Hu, Z. Liu, and M. Zuo, "Controls of distinct mineral compositions on pore structure in over-mature shales: a case study of lower cambrian niutitang shales in South China," *Minerals*, vol. 11, no. 1, p. 51, 2021.
- [14] K. Jiao, S. P. Yao, C. Li, H. Wu, M. C. Li, and Z. Y. Tang, "The characterization and quantitative analysis of nanopores in unconventional gas reservoirs utilizing FESEM-FIB and image processing: an example from the lower Silurian Longmaxi shale, upper Yangtze region, China," *International Journal of Coal Geology*, vol. 128, pp. 1–11, 2014.
- [15] W. M. Ji, Y. Song, Z. X. Jiang et al., "Estimation of marine shale methane adsorption capacity based on experimental investigations of lower Silurian Longmaxi formation in the Upper Yangtze Platform, South China," *Marine and Petroleum Geology*, vol. 68, pp. 94–106, 2015.
- [16] P. F. Wang, Z. X. Jiang, W. M. Ji et al., "Heterogeneity of intergranular, intraparticle and organic pores in Longmaxi shale in Sichuan Basin, South China: evidence from SEM digital images and fractal and multifractal geometries," *Marine and Petroleum Geology*, vol. 72, pp. 122–138, 2016.
- [17] K. L. Xi, Y. C. Cao, B. G. Haile et al., "How does the pore-throat size control the reservoir quality and oiliness of tight sandstones? The case of the Lower Cretaceous Quantou Formation in the southern Songliao Basin, China," *Marine and Petroleum Geology*, vol. 76, pp. 1–15, 2016.
- [18] H. Gao and H. Z. Li, "Determination of movable fluid percentage and movable fluid porosity in ultra-low permeability sandstone using nuclear magnetic resonance (NMR) technique," *Journal of Petroleum Science and Engineering*, vol. 133, pp. 258–267, 2015.
- [19] L. Xiao, Z. Q. Mao, C. C. Zou, Y. Jin, and J. C. Zhu, "A new methodology of constructing pseudo capillary pressure (P_c) curves from nuclear magnetic resonance (NMR) logs," *Journal of Petroleum Science and Engineering*, vol. 147, pp. 154–167, 2016.
- [20] Y. Liu, Y. B. Yao, D. M. Liu, S. J. Zheng, G. X. Sun, and Y. H. Chang, "Shale pore size classification: an NMR fluid typing method," *Marine and Petroleum Geology*, vol. 96, pp. 591–601, 2018.
- [21] F. S. J. Martínez, M. A. Martín, F. J. Caniego et al., "Multifractal analysis of discretized X-ray CT images for the characterization of soil macropore structures," *Geoderma*, vol. 156, no. 1–2, pp. 32–42, 2010.
- [22] Y. Wang, J. Pu, L. H. Wang et al., "Characterization of typical 3D pore networks of Jiulaodong formation shale using nano-transmission X-ray microscopy," *Fuel*, vol. 170, pp. 84–91, 2016.
- [23] T. F. Zhang, S. Y. Xie, Z. Y. Bao, Y. Wang, and L. Y. Pan, "Fractal and multifractal research on pore system for porous dolomite reservoirs based on high-resolution CT," *Bulletin of Geological Science and Technology*, vol. 35, no. 6, pp. 56–61, 2016.
- [24] S. J. Zheng, Y. B. Yao, D. M. Liu, Y. D. Cai, Y. Liu, and X. W. Li, "Nuclear magnetic resonance T_2 cutoffs of coals: a novel method by multifractal analysis theory," *Fuel*, vol. 241, pp. 715–724, 2019.
- [25] W. Li, H. F. Liu, and X. X. Song, "Multifractal analysis of Hg pore size distributions of tectonically deformed coals," *International Journal of Coal Geology*, vol. 144–145, pp. 138–152, 2015.
- [26] K. Liu and M. Ostadhassan, "Quantification of the microstructures of Bakken shale reservoirs using multi-fractal and lacunarity analysis," *Journal of Natural Gas Science and Engineering*, vol. 39, pp. 62–71, 2017.
- [27] M. M. Labani, R. Rezaee, A. Saeedi, and A. A. Hinai, "Evaluation of pore size spectrum of gas shale reservoirs using low pressure nitrogen adsorption, gas expansion and mercury porosimetry: a case study from the Perth and Canning basins, western Australia," *Journal of Petroleum Science and Engineering*, vol. 112, pp. 7–16, 2013.
- [28] S. Liu, W. Ma, L. Jansa, W. Huang, X. Zeng, and C. Zhang, "Characteristics of the shale gas reservoir rocks in the Lower Silurian Longmaxi Formation, East Sichuan Basin, China," *Energy Exploration & Exploitation*, vol. 31, no. 2, pp. 187–219, 2013.
- [29] N. Yang, S. H. Tang, S. H. Zhang, and J. J. Yi, "Evaluation shale pore size spectrum using mercury porosimetry and nitrogen adsorption experiment: a case study from the longtan formation shale, southeastern Hunan, China," *Advanced Materials Research*, vol. 962–965, pp. 34–40, 2014.
- [30] Z. Q. Ouyang, D. M. Liu, Y. D. Cai, and Y. B. Yao, "Investigating the fractal characteristics of pore-fractures in bituminous coals and anthracites through fluid flow behavior," *Energy & Fuels*, vol. 30, no. 12, pp. 10348–10357, 2016.
- [31] Q. Q. Dai, G. W. Wang, C. J. Lu et al., "Occurrence characteristics and controls over mobile fluids in a tight sandstone reservoir," *Australian Journal of Earth Sciences*, vol. 65, no. 6, pp. 877–887, 2018.
- [32] C. G. Huang, X. Guan, X. L. Ni, H. Y. Chang, S. M. Zhang, and S. Yang, "The characteristics and major factors controlling on the E_3^2 dolomite reservoirs in saline lacustrine basin in the Yingxi area of Qaidam Basin," *Natural Gas Geoscience*, vol. 28, no. 2, pp. 219–231, 2017.
- [33] D. Q. Chen, X. S. Shen, J. Cui, Y. P. Lu, and Y. Huang, "Reservoir characteristics and controlling factors of deep diamictite

- in Yingxi area, Qaidam Basin,” *Lithologic Reservoirs*, vol. 27, no. 5, pp. 212–215, 2015.
- [34] J. Liu, C. L. Liu, Q. Dong, P. Sun, L. Zhang, and Z. Guo, “A study of the period of the gas accumulation of Paleogene-Neogene in Western Qaidam Basin,” *Earth Science Frontiers*, vol. 23, no. 5, pp. 127–134, 2016.
- [35] E. H. Rios, I. Figueiredo, A. K. Moss et al., “NMR permeability estimators in ‘chalk’ carbonate rocks obtained under different relaxation times and MICP size scalings,” *Geophysical Journal International*, vol. 206, no. 1, pp. 260–274, 2016.
- [36] P. Q. Zhao, Z. L. Wang, Z. C. Sun, J. C. Cai, and L. Wang, “Investigation on the pore structure and multifractal characteristics of tight oil reservoirs using NMR measurements: Permian Lucaogou Formation in Jimusaer sag, Junggar Basin,” *Marine and Petroleum Geology*, vol. 86, pp. 1067–1081, 2017.
- [37] F. J. Caniego, M. A. Martí, and F. San José, “Renyi dimensions of soil pore size distribution,” *Geoderma*, vol. 112, no. 3–4, pp. 205–216, 2003.
- [38] J. P. Ferreira and E. V. Vázquez, “Multifractal analysis of Hg pore size distributions in soils with contrasting structural stability,” *Geoderma*, vol. 160, no. 1, pp. 64–73, 2010.
- [39] H. L. Wang, H. F. Liu, W. Li, and Y. L. Yang, “Multifractal characterization of tectonically deformed coal pore structure based on mercury injection technology,” *Safety in Coal Mines*, vol. 47, no. 1, pp. 33–37, 2016.
- [40] M. G. Hu, J. F. Wang, and Y. Ge, “Super-resolution reconstruction of remote sensing images using multifractal analysis,” *Sensors*, vol. 9, no. 11, pp. 8669–8683, 2009.
- [41] M. E. Ramia and C. A. Martín, “Sedimentary rock porosity studied by electromagnetic techniques: nuclear magnetic resonance and dielectric permittivity,” *Applied Physics A Materials Science & Processing*, vol. 118, no. 2, pp. 769–777, 2015.
- [42] Y. D. Cai, D. M. Liu, Z. J. Pan, Y. B. Yao, J. Q. Li, and Y. K. Qiu, “Pore structure and its impact on CH₄ adsorption capacity and flow capability of bituminous and subbituminous coals from Northeast China,” *Fuel*, vol. 103, pp. 258–268, 2013.
- [43] Q. Q. Dai, G. W. Wang, X. Zhao et al., “Fractal model for permeability estimation in low-permeable porous media with variable pore sizes and unevenly adsorbed water lay,” *Marine and Petroleum Geology*, vol. 130, article 105135, 2021.
- [44] Y. R. Fan, J. Y. Liu, X. M. Ge, S. G. Deng, H. L. Liu, and D. N. Gu, “Permeability evaluation of tight sandstone based on dual T₂ cutoff values measured by NMR,” *Chinese Journal of Geophysics*, vol. 61, no. 4, pp. 1628–1638, 2018.
- [45] H. Daigle, B. Thomas, H. Rowe, and M. Nieto, “Nuclear magnetic resonance characterization of shallow marine sediments from the Nankai trough, integrated ocean drilling program expedition 333,” *Journal of Geophysical Research: Solid Earth*, vol. 119, no. 4, pp. 2631–2650, 2014.
- [46] A. S. Ziarani and R. Aguilera, “Pore-throat radius and tortuosity estimation from formation resistivity data for tight-gas sandstone reservoirs,” *Journal of Applied Geophysics*, vol. 83, pp. 65–73, 2012.
- [47] D. Davudov and R. G. Moghanloo, “A new model for permeability impairment due to asphaltene deposition,” *Fuel*, vol. 235, pp. 239–248, 2019.
- [48] W. M. Ji, Y. Song, Z. X. Jiang et al., “Fractal characteristics of nano-pores in the Lower Silurian Longmaxi shales from the Upper Yangtze Platform, South China,” *Marine and Petroleum Geology*, vol. 78, pp. 88–98, 2016.
- [49] M. Wang, H. Xue, S. Tian, R. W. Wilkins, and Z. Wang, “Fractal characteristics of Upper Cretaceous Lacustrine shale from the Songliao Basin, NE China,” *Marine and Petroleum Geology*, vol. 67, pp. 144–153, 2015.
- [50] T. C. Halsey, M. H. Jensen, L. P. Kadanoff, I. Procaccia, and B. I. Shraiman, “Fractal measures and their singularities: the characterization of strange sets,” *Nuclear Physics B - Proceedings Supplements*, vol. 33, no. 2, pp. 1141–1151, 1986.